Diamond & Related Materials 30 (2012) 20–30

Contents lists available at SciVerse ScienceDirect

Diamond & Related Materials

journal homepage: www.elsevier.com/locate/diamond

Quantitative characterization of plastic deformation of single diamond crystals: A high pressure high temperature (HPHT) experimental deformation study combined with electron backscatter diffraction (EBSD)

D. Howell [a,b,*], S. Piazolo [b,c], D.P. Dobson [a], I.G. Wood [a], A.P. Jones [a], N. Walte [d], D.J. Frost [d], D. Fisher [e], W.L. Griffin [b]

[a] Department of Earth Sciences, University College London, Gower Street, London, WC1E 6BT, UK
[b] ARC Centre of Excellence for Core to Crust Fluid Systems (CCFS) and GEMOC, Department of Earth and Planetary Science, Macquarie University, NSW 2109, Australia
[c] Department of Geological Sciences, Stockholm University, SE-10691 Stockholm, Sweden
[d] Bayerisches Geoinstitut, Universität Bayreuth, D-95440, Bayreuth, Germany
[e] Diamond Trading Company, DTC Research Centre, Belmont Road, Maidenhead, SL6 6JW, UK

ARTICLE INFO

Article history:
Received 3 July 2012
Received in revised form 14 September 2012
Accepted 17 September 2012
Available online 25 September 2012

Keywords:
Diamond
D-DIA
Strain-induced birefringence
Brown pink colour
Deformation twinning
Electron back scatter diffraction (EBSD)

ABSTRACT

We report the results of a high-pressure high-temperature (HPHT) experimental investigation into the deformation of diamonds using the D-DIA apparatus. Electron backscatter diffraction (EBSD) data confirm that well-defined 300–700 nm wide {111} slip lamellae are in fact deformation micro-twins with a 60° rotation around a <111> axis. Such twins formed at high confining pressures even without any apparatus-induced differential stress; mechanical anisotropy within the cell assembly was sufficient for their formation with very little subsequent lattice bending (<1° per 100 μm). When apparatus-induced differential stresses were applied to diamonds under HPHT conditions, deformation twin lamellae were generated, and continuous and discontinuous crystal lattice bending occurred (4–18° per 100 μm), including bending of the {111} twin lamellae. The {111}<011> slip system dominates as expected for the face-centred cubic (FCC) structure of diamond. Slip occurs on multiple {111} planes resulting in rotation around <112> axes. Deformation microstructure characteristics depend on the orientation of the principal stress axes and finite strain but are independent of confining pressure and nitrogen content. All of the uniaxially deformed samples took on a brown colour, irrespective of their initial nitrogen characteristics. This is in contrast to the two quasi-hydrostatic experiments, which retained their original colour (colourless for nitrogen free diamond, yellow for single substitutional nitrogen, Type Ib diamond) despite the formation of {111} twin lamellae. Comparison of our experimental data with those from two natural brown diamonds from Finsch mine (South Africa) shows the same activation of the dominant slip system. However, no deformation twin lamellae are present in the natural samples. This difference may be due to the lower strain rates experienced by the natural samples investigated. Our study shows the applicability and potential of this type of analysis to the investigation of plastic deformation of diamonds under mantle conditions.

1. Introduction

Diamonds, along with the mineral and fluid inclusions that they may carry, represent the deepest samples of the Earth's mantle that can be found at the surface [1]. Their economic and scientific importance means that they are one of the most intensively studied minerals. Diamond crystals show a range of different morphologies, growth mechanisms, colours and textures, all of which can affect their economic value. Some of these characteristics are interdependent, for example brown and pink colours in diamonds have long been recognized to be associated with plastic deformation [2]. Often, the brown or pink colour is only observed in lamellae parallel to the {111} planes while the bulk of the diamond is colourless [3]; this feature commonly is referred to as "graining".

As observed in other face-centred cubic (FCC) materials, the main slip system in diamond is {111} <110>. This means that the {111} planes are the active slip planes with movement in the <110> directions. In diamond, the {111} planes are also the twin planes. Twins in diamonds can be created during growth (seen in natural diamonds [4,5] and high-pressure high-temperature (HPHT) experiments [6]) or induced by deformation [7]. In deformation experiments performed on diamonds under vacuum at high temperature [8] as well as at high pressure and high temperature (HPHT; [9]), the {111} lamellae produced

* Corresponding author at: ARC Centre of Excellence for Core to Crust Fluid Systems (CCFS) and GEMOC, Department of Earth and Planetary Science, Macquarie University, NSW 2109, Australia. Tel.: +61 298504401.
E-mail address: daniel.howell@mq.edu.au (D. Howell).

0925-9635/$ – see front matter © 2012 Elsevier B.V. All rights reserved.
http://dx.doi.org/10.1016/j.diamond.2012.09.003

were identified as deformation twins. This occurrence of deformation twin lamellae was then confirmed in natural samples by Varma [10]. Despite this finding being criticised in a review by Orlov [11], recent transmission electron microscopy (TEM) work on both experimentally deformed [12] and naturally deformed diamonds [13] has confirmed the presence of these {111} deformation twin lamellae.

Traditionally, the primary indication that a diamond has been subject to plastic deformation has been the occurrence of macroscopically visible slip planes/deformation twin lamellae that occur parallel to {111} faces, as well as brown colouration. Only relatively recently has the quantification of deformation characteristics in diamonds, encompassing scales from nm to mm, becomes possible due to the development of the SEM-based electron backscatter diffraction analysis (EBSD) technique [14,15]. A significant benefit of EBSD analysis over TEM work is that it does not require the preparation of very thin (~5 μm thick) slices of material; EBSD simply requires a suitably polished surface. Once deformation can be quantified through EBSD analysis, relationships between deformation features and other optical and chemical characteristics (e.g. Cathodoluminescence (CL), Secondary Electron (SE) and birefringence imaging, Raman and infrared (IR) mapping) can be established, offering new avenues of data interpretation. CL is often imaged to observe variations in defect concentrations that can highlight a sample's growth stratigraphy [16,17] as well as any defects related to deformation i.e. slip planes [13]. SE imaging is restricted to showing surface topography and morphological variations that may be induced by deformation or subsequent damage, while birefringence is the result of strain-induced optical anomalies [18]. Raman mapping can be used to qualitatively identify strain in the diamond lattice [13,19,20], and IR mapping can resolve the spatial distribution of impurities, in particular nitrogen and its aggregation state [21–24].

There are obvious benefits in establishing causal links between characteristics that can be measured by different techniques. Furthermore, if we can experimentally deform diamonds at mantle conditions e.g. >4 GPa and >1200 °C, it will be possible to establish how diamond deforms under different P-T and strain-rate conditions. As in systematic studies conducted on other geological material and metals [25], such experiments can be combined with detailed analysis of rheological behaviour and the developing microstructures [12], to interpret the deformation and its links to the chemical history of the diamond. All of this will allow us to make inferences about Earth's otherwise inaccessible mantle.

An additional important implication of plastic deformation for diamond studies is the possible effect it can have on the rate of nitrogen aggregation. Presently, the rate at which nitrogen atoms aggregate with other nitrogen atoms is used to estimate either how long a diamond has resided in the mantle, or the temperature at which it has resided [26,27]. This technique must assume that the aggregation process occurs at a known rate. A common misconception is that plastic deformation simply increases the rate of nitrogen aggregation. However, HPHT experiments investigating the effects of microstructure on impurity diffusion in diamonds have shown that the relationship between deformation (and resultant microstructure) and the rate of nitrogen aggregation is unclear [12]. Byrne et al. [28] have presented a theory as to how plastic deformation could lead to the break up of B centres (4 nitrogen atoms surrounding a vacancy) and create a variety of N3 (N_3–V), H3 (N–V–N) and single nitrogen centres. Therefore use of the simple age/temperature relationship for nitrogen aggregation in diamond should be used with extreme caution, especially in samples that exhibit evidence of plastic deformation.

EBSD has been applied to studying polycrystalline synthetic diamond [29,30] but to our knowledge, it has not been applied to the quantitative investigation of plastic deformation in experimentally deformed diamond. Recently, a variety of deformation features in polycrystalline diamondite were recognised utilizing EBSD [31,32], emphasising that experimental data are needed to interpret the deformation structures seen in diamond and in diamond aggregates.

Here we report a pilot study, combining a new method of deforming diamonds under HPHT conditions in a deformation DIA (D-DIA, a modified cubic-anvil press [33]), and using EBSD to quantitatively analyse the deformation that has occurred. Deformation data are compared to a range of imaging techniques, including CL, SE and birefringence imaging using the MetriPol system [34]. For comparative purposes, two naturally deformed brown diamonds are analysed by these methods as well. The results show that the D-DIA technique can deform diamonds at temperatures and pressures relevant to nature, and demonstrate the usefulness of EBSD analysis for the quantitative investigation of plastic deformation in diamonds. The observed microstructures include deformation twinning, gradual crystal bending and continuous and discontinuous discrete high- and low-angle boundaries.

2. Samples

Seven single-crystal synthetic diamonds (provided by DTC Maidenhead) were used in the HPHT experiments described below (Table 1). The reason for using synthetic diamonds was to reduce the likelihood that the samples already contained any internal strain and/or plastic deformation. The lack of residual stress and strain was confirmed by birefringence imaging. Three samples (DD192, DD194 and DD197) were yellow Type Ib (containing 100–150 ppm single-substitutional, un-aggregated nitrogen), with their three sets of orthogonal faces parallel to {100}. The other four samples were colourless Type IIa (nominally nitrogen-free, i.e. <10 ppm). DD193, DD196 and DD198 have one pair of faces parallel to (100), and two sets of faces parallel to {110}. Sample DD195 had one pair of faces parallel to (111), one pair parallel to $(-1\bar{1}2)$ and the final pair parallel to $(1\bar{1}0)$. All seven samples initially were approximately 1 mm cubes.

Two natural samples have also been analysed to compare their characteristics with those generated during the HPHT experiments. Both are from the private collection of Dr H. Judith Milledge (UCL); they are brown diamonds from the Finsch mine, South Africa. FJM01, of rounded dodecahedral morphology, showed obvious growth layering on its surface, probably revealed by dissolution, while FJM02 appeared to be a broken fragment of a larger stone. Both samples are approximately 1 mm in size. Facets were mechanically polished on both samples

Table 1
Description of the samples prior to experiments and the conditions they were subjected to. The details of the crystals' orientation within the experimental assemblies are also provided.

Run #	Diamond type	Starting colour	P (GPa)	T (°C)	Strain rate (s^{-1})	Crystal faces Uniaxial stress applied to	Side crystal faces
DD192	Ib	Yellow	7.3	~1700	0	(100)	(010), (001)
DD193	II	Colourless	7.3	~1700	0	(100)	(011), $(0\bar{1}1)$
DD194	Ib	Yellow	7.3	~1700	0.000024	(100)	(011), $(0\bar{1}1)$
DD195	II	Colourless	7.3	~1800	0.000028	(110)	$(1\bar{1}1)$, $(1\bar{1}2)$
DD196	II	Colourless	5.1	~1800	0.000029	(100)	(011), $(0\bar{1}1)$
DD197	Ib	Yellow	5.1	~1800	0.000030	(100)	(010), (001)
DD198	II	Colourless	5.1	~1800	0.000057	(100)	(011), $(0\bar{1}1)$

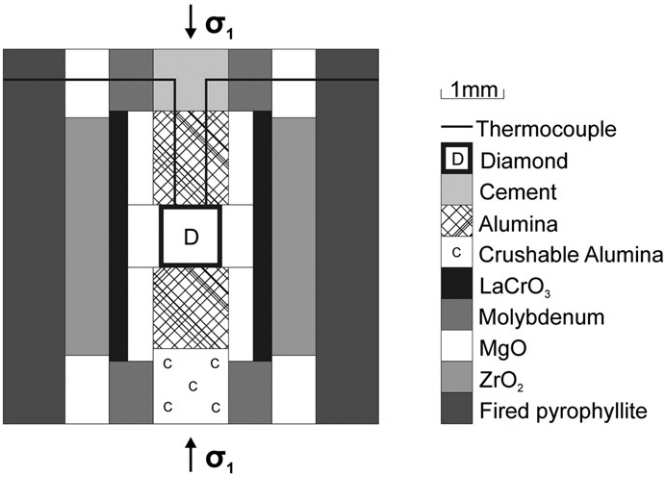

Fig. 1. Diagram showing the cell assembly used in the D-DIA experiments. Arrows labelled with σ_1 indicate direction of the two differential rams that apply the uniaxial stress to the Set II experiments. The two horizontal pieces of the thermocouple wire are actually encased within an alumina tube, which are placed within a groove cut into the surrounding cell assembly.

to allow EBSD analysis to be performed. On FJM01 one face was polished roughly parallel with a (100) crystal face, while on FJM02 two non-parallel faces were polished on the natural fracture planes. The brown colour in both samples is homogeneous and does not show obvious graining.

3. Experimental techniques

The HPHT experimental apparatus used was the deformation DIA (D-DIA; Bayerisches Geoinstitut (BGI), Bayreuth, Germany). The reason for using the D-DIA is that it contains two additional rams positioned in the upper and lower guide blocks of the original DIA apparatus. This allows the application of an independent uniaxial stress to samples that are already under HPHT conditions. This is in contrast to all previous HPHT diamond deformation experiments that have relied solely on mechanical anisotropy within the cell assembly with the application of hydrostatic pressure.

The cell assembly devised for this set of experiments used a 6 mm fired pyrophyllite cube compressed using 4-mm edge-length tungsten carbide anvils (Fig. 1). The approach adopted for these experiments was to create a pronounced mechanical anisotropy within the cell assembly, placing alumina pistons above and below the sample so that the cell would be significantly stiffer in the orientation of the applied stress. The strain rate values given (Table 2) are those imposed on the cell assembly, they are not calculated from the deformation partitioned into the diamond. The series of experiments was split into two sets. Set I consists of two experiments, one with each diamond type (DD192 and DD193), which were performed at high temperature and high confining pressure and subsequently cooled and decompressed. Even though no differential stress was applied to the cell assembly, an average strain of 2.6% (Table 2) was observed in the two diamonds, as determined by measuring the crystal dimensions before and after the experiment. Thus, these experiments represent "near" hydrostatic experiments. Set II consisted of uniaxially deformed tests. The differential rams were introduced at a constant cell strain rate of approximately 3×10^{-5} s^{-1} or 6×10^{-5} s^{-1}. These strain rates are much greater than the strain rates that are thought to occur naturally in the uppermost mantle (10^{-15} s^{-1} [35]) but this choice of parameters reflects experimental time constraints. See Table 1 for details of the conditions for each experiment.

The procedure for all the experiments was as follows. The cells were taken up to pressure (P) over a period of 3 h. Once at pressure, they were taken to high temperature (T) by resistive heating using a lanthanum chromate furnace, over approximately 10 min. Once at pressure and temperature, the Set I experiments were maintained for 4 h before being quenched and decompressed overnight (*ca* 10 h), using the computer controlled system. For Set II, once the samples were at P and T, the uniaxial stress was applied by the advancement of the differential ram for 4 h. Due to the introduction of the differential ram, the system had to be manually decompressed after quenching. As a result, this decompression was performed over a shorter time frame of approximately 90 min.

The pressure and temperature conditions used for these experiments were *ca* 5.1 and 7.3 GPa, and between 1700 and 1800 °C. These high temperatures allowed the thermodynamically driven processes to occur within the relatively short duration of the experiment but are higher than the actual mantle temperatures expected at the pressures used (1100 °C and 1300 °C respectively). For all experiments except DD195, samples were oriented in the cell so that the uniaxial stress was applied to a pair of {100} faces, i.e. along a [100] direction. In experiment DD195 the diamond was oriented with the compression direction parallel to [110]. The samples were recovered by cutting open the cell assembly. All the diamonds were acid washed prior to any analysis, to make sure that any material from the cell was removed. This means that if any graphitization occurred during the lower-pressure experiments (i.e. those outside the diamond stability field) it was not documented.

4. Analytical techniques

All seven experimental samples were optically analysed both before and after being deformed. Prior to the experiments, MetriPol and bulk-IR analyses were performed. After the experiments, MetriPol and

Table 2
Summary of the main results from the D-DIA experiments. The values of strain are given as percentages and represent the average of two different calculations. The first is obtained by dividing the change in length (parallel to the compression axis) by the original length. The second is calculated by dividing the change in cross-sectional area (perpendicular to the compression axis) by the recovered cross-sectional area. In a sample that retained its integral cube shape, the strain measure in one dimension would be equal to a negative value of the measure of strain in two dimensions. For the sake of the average strain value presented here, the negative nature of the two-dimensional strain measurement is ignored. The amount of crystal bending per 100 μm was recorded by the EBSD analyses. Nitrogen aggregation is a measure of transformation from C centres to A centres, given in percent of total nitrogen as A centres. DTL = deformation twin lamellae, DF = decompression fracture, BF = brittle fracture, MDF = major decompression fracture, EP = etch pits.

Run #	Final colour	Average strain (%)	Crystal bending per 100 μm (degrees)	Nitrogen aggregation (% IaA)	Deformation features
DD192	Yellow	2.6	0.8	0%	DTL, DF
DD193	Colourless	–	–	–	DTL, DF, BF
DD194	N/R	–	–	N/R	MDF
DD195	Brown	4.4	1.2–10	–	DTL, BF
DD196	Brown	5.5	1–7	–	DTL, DF, EP
DD197	Brown	4.3	Up to 4	37%	DTL, BF
DD198	Brown	6.1	Up to 18	–	DTL, BF

IR analyses were repeated, along with SE and CL imaging in a scanning electron microscope (SEM). IR spectra along with SE and CL images were also collected on the two natural diamonds. EBSD orientation-contrast images were collected on all of the diamonds presented in this study.

The MetriPol birefringence system used in this study is fitted to a Leica DMLP microscope (Department of Earth Sciences, University College London, UK). All analyses presented in this study were recorded using 550 nm wavelength light filters. Single bulk IR spectra were collected on each experimental sample using a Nicolet Magna IR 750 FTIR spectrometer (DTC Research Center, Maidenhead, UK). Nitrogen concentrations and aggregation states were calculated using the CAXBD97.xls spreadsheet. IR analysis on the natural samples was performed using a Nicolet iN10 spectrometer (GEMOC, Macquarie University, Australia) and deconvoluted using the same spreadsheet. The SE and monochrome CL images were collected on a Zeiss EVO 15 SEM (GEMOC, Macquarie University, Australia). Accelerating voltages were varied between 15 and 25 kV to obtain the best quality images. The samples were cleaned and carbon-coated prior to imaging.

Full crystallographic orientation data were obtained from automatically indexed EBSD patterns collected on a Philips XL-30-ESEM-FEG (Department of Geological Sciences, Stockholm University, Sweden) and on a Zeiss Ultra Plus (University of Sydney, Australia). EBSD analyses were carried out directly on the experimental samples without further polishing. Working conditions during acquisition of EBSD patterns were 20 kV and 25 kV accelerating voltage, ~0.8 nA beam current, working distance of about 20 mm, 70° sample tilt, and low-vacuum mode (0.3–0.4 Torr) (Stockholm University) and at high vacuum mode (samples carbon coated, University of Sydney). Patterns were acquired on rectangular grids by moving the electron beam at a regular step size of 0.05, 0.1, 1, 1.5 and 2 μm depending on the structures to be quantified. EBSD patterns were indexed using CHANNEL 5 software from HKL Technology–Oxford Instruments. The electron backscatter diffraction patterns from the diamond were automatically indexed by comparing the observed reflector intensities with those of theoretical reflectors. For this procedure, we compared to 50 theoretically calculated reflectors. In addition, high-resolution orientation contrast (OC) images were taken [36].

Processing of the EDSB data was performed as follows. Firstly, noise reduction is carried out by replacing the non-indexed solutions by the most-common-neighbour orientation, following the procedure tested by Prior et al. [36] and Bestmann and Prior [37]. We present the resulting data in the form of pole figures and colour-coded maps. The crystallographic orientations of lattice directions and planes are plotted on the upper hemisphere of the equal-area stereographic projection. For map representation, misorientation angles between neighbouring data points have been grouped into low-angle boundaries of 1–2°, 2–5° and 5–10° misorientation and high-angle boundaries (misorientation > 10°). Crystallographic misorientations are mainly investigated using misorientation profiles, misorientation angle histograms and dispersion paths on pole figures (see below for details). Among all the combinations of symmetrically equivalent axis/angle pairs, we followed the general convention to select the pair with the minimum misorientation angle [38].

Boundary trace analysis [36,39–41] was used to constrain the possible active slip systems as well as the orientation of boundaries in terms of crystallography. Boundary trace analysis is a powerful method for determining the most feasible geometry of a low-angle boundary and the active slip system(s). This technique considers the 2D trace of a low-angle boundary on the EBSD map and the dispersion of the orientation data around a rotation axis for an area sampled across the boundary itself. In the case of a tilt boundary, the boundary plane must contain the two-dimensional boundary trace and the rotation axis [40]. The latter is identified on the pole figures as the direction with no or little dispersion. A plane at high angle to the boundary plane and containing the rotation axis represents the most likely active slip plane and must contain the slip direction. In the case of a twist boundary, the rotation axis must be orthogonal to the boundary plane.

5. Results

5.1. Experimentally deformed samples

The two experiments in Set I (i.e. quasi-hydrostatic) have largely retained their initial straight-edged appearance but experienced some decompression fracturing. While only a small portion of the top of DD192 fractured off (Fig. 2A), DD193 broke in half (Fig. 2J). CL imaging reveals that both samples contain two distinct sets of macroscopically visible lamellae that are perpendicular to each other (Fig. 2B and C). SE images show that individual lamellae form slight elevations or depressions on the surface (Fig. 2D). The lamellae are between 0.3 and 0.5 μm wide and are very well defined through EBSD as perfect micro twins, with {111} being the twin and simultaneous slip plane and a systematic rotation of 60° about the <111> direction (Fig. 2E–G). The distance between individual lamellae ranges from ~1 to 20 μm. Continuous bending of the crystal lattice between the twin/slip lamellae occurs to a minor extent and is less than 0.8° per 100 μm (Fig. 2H). Crystallographic, CL and SE characteristics of sample DD193 are identical to that of DD192. DD192 has retained its yellow colour and IR analysis reveals no detectable nitrogen aggregation. DD193 has maintained its colourless appearance. First-order birefringence colours are now observed in DD192 but the pattern observed with the MetriPol does not correlate specifically with the lamellae seen on the surface (Fig. 2J). We suggest that this is due to the fact that the MetriPol analysis was not performed parallel to the lamellae but at an oblique angle, so the strain fields being analysed will relate to the multiple lamellae occurring in the beam path.

Of the five experiments in Set II (uniaxially deformed), one (DD194) was recovered in many broken pieces and as a result, it was not in a suitable condition for any post-experimental analyses to be performed. Uniaxial deformation of sample DD195 produced a strain of 4.4%, resulting in a macroscopically noticeable modification of the original straight-edged cube (Fig. 3A). In the recovered sample, the two faces perpendicular to σ_1 are now concave, while the four side faces have remained relatively straight-edged. It has also undergone some minor fracturing. The sample is no longer colourless but has acquired a fairly homogenous brown colour (Fig. 3A). Strain-induced birefringence is clearly seen and shows a pattern of intersecting bands at ~67° (Fig. 3B). Locally, twin lamellae similar to those observed in the samples recovered from the experiments in Set I are present (red arrow, Fig. 3C). However, it is clear that they are no longer straight but appear bent. Crystal lattice distortions vary from 1.2° to 10° per 100 μm. Less crystal bending is seen close to the remaining straight edges (e.g. area 1 in Fig. 3), while most intense bending is seen in the centre (area 2 in Fig. 3) and close to the bowed sides of the sample (areas 3 and 4 in Fig. 3). In area 1 (Fig. 3), crystal bending is relatively continuous with no distinct low-angle boundaries and dominant rotation axes. In areas 2 and 3 (Fig. 3) subgrain boundaries can be continuous over several 10 s of μm and mainly follow a conjugate set of {111}. Rotation axes are always [112], but the specific axis changes according to the orientation of the slip plane and position within the sample (Fig. 3D).

Sample DD196 experienced decompression fracturing similar to that seen in DD192, resulting in a serrated top surface. It has also lost its original straight-edged form and the surface (100) that is perpendicular to σ_1 is now significantly bowed (Fig. 4A). The diamond has changed from colourless to a homogenous brown colour, slightly paler than that seen in DD195 (Fig. 4A). Two distinct sets of {111} slip lamellae are at ~70° to each other, while one of them forms the expected 54° angle to the stressed (100) face. Macroscopically, slight bending of these lamellae can be observed (Fig. 4A and B). The diamond now contains strain-induced birefringence with parts of the

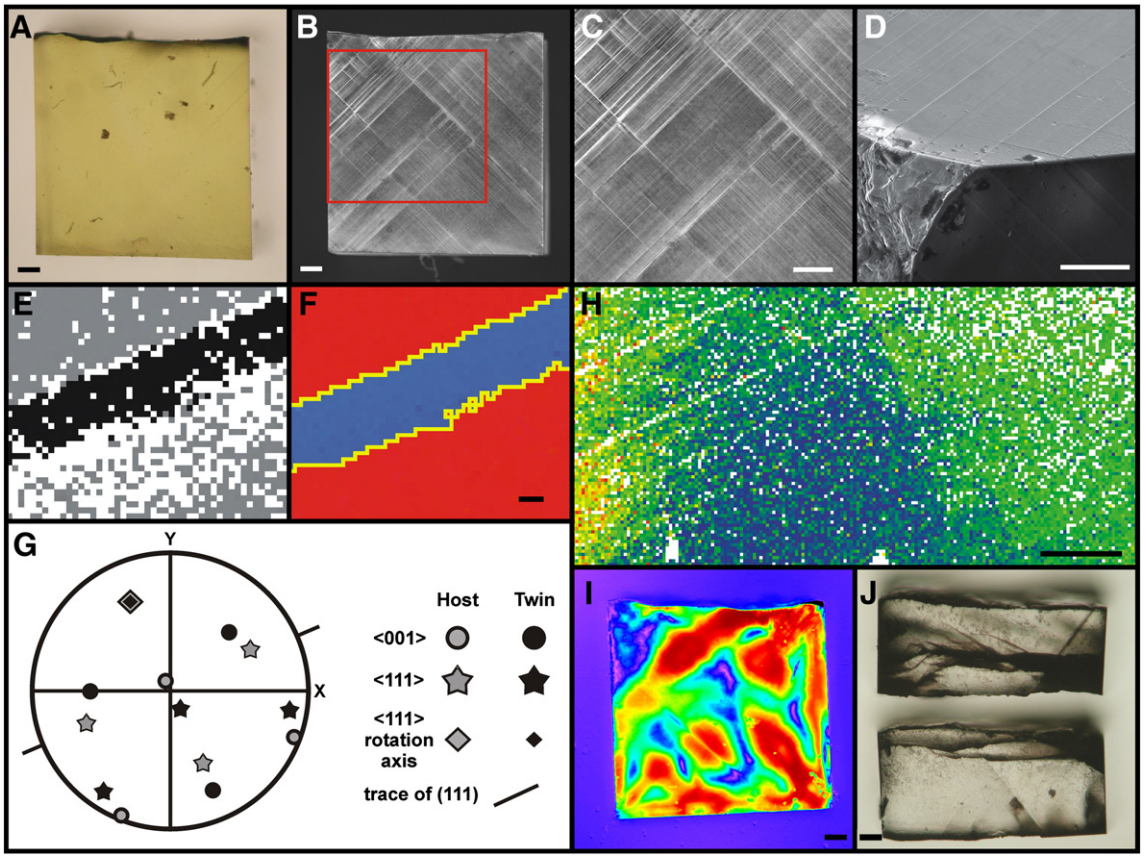

Fig. 2. Images and EBSD data of samples recovered from the Set I (quasi-hydrostatic) experiments with (001) as the viewing surface for sample DD192 (A–I) and (110) for DD193 (J). (A) Photo of DD192 taken under unpolarized light. (B) CL image of the same crystal face shown in (A), note the frequency of lamellae and their 90° angle to each other. (C) Close-up of CL image; area corresponds to the red box in (B); note the 0.5–3 μm offsets along one set of slip planes. (D) SE image showing the lamellae and how they can be traced onto adjacent crystal faces; note that lamellae are characterized by topographic depressions, elevations and offsets. (E) Map of twin analysis using EBSD (raw data; 0.05 μm step size), grey and black refer to host and twin orientation, twin width is approximately 0.3 μm; non-indexed points are white. (F) Processed EBSD data showing host in red and twin in blue with the two parallel twin boundaries (yellow) marked; these are defined as a 60° rotation around <111>. (G) Pole figure (upper hemisphere, equal area projection) showing twin relationship; note that one <111> axis of the host and twin overlap perfectly indicating rotation around this axis, also the pole to the (111) plane that is parallel to the twin boundary. (H) EBSD map over a large part of the sample showing in blue to red a change in orientation of 2° (raw data, 2 μm step size); deformation twins are disregarded here; note the gentle bend of the crystal. (I) MetriPol |sin (δ)| analysis of DD192 performed through the crystal face shown in (A). (J) Photo of DD193 taken under plane light. Scale bars in images (A), (B), (C), (I) and (J) represent 100 μm, 20 μm in image (D), 0.2 μm in (E) and (F), and 50 μm in image (H).

pattern appearing parallel to the slip lamellae (Fig. 4B). EBSD analysis reveals that, as in DD195 (Fig. 3), continuous lattice distortions as well as distinct subgrain boundaries with misorientation of 1–2° are present. Depending on the location relative to the principal stress axis and stressed face, lattice distortions vary between 1° and 7° per 100 μm (Fig. 4D–G). Slip planes are recorded in the {111} orientation, and lattice rotations occur in two specific <112> directions depending on the activated {111} plane (Fig. 4H).

DD197 has also lost its original straight-edged shape (Fig. 5A), and its colour has changed from yellow to a homogenous brown of similar intensity to that seen in DD195. A significant strain-induced birefringence pattern has also formed (Fig. 5B). In the CL image, slip planes and twin lamellae are clearly visible, and some minor fractures have developed (Fig. 5C). Lattice bending does not exceed 4° per 100 μm (Fig. 5E). Slip has again occurred on a set of two {111} planes at an angle of ~70° to each other, with rotations around different axes, one <112> axis and one <011> axis (Fig. 5F–I). IR analysis shows that around 37% of the nitrogen in DD197 has aggregated from C centres to A centres.

Sample DD198 contains two sets of abundant curved slip planes; it shows some minor fracturing and has lost its original straight-edged shape (Fig. 6A–D). The sample has changed from colourless to a brown similar to DD195 and DD197. It has also developed significant strain-induced birefringence (Fig. 6B). EBSD analysis reveals up to 18° of misorientation per 100 μm. High misorientations are seen in the centre of the sample, with less deformation close to the straight faces (Fig. 6E). Boundaries show misorientation angles of up to 12°, thus forming new grain boundaries. Lamellae are bent but still sub-parallel to two sets of {111} planes with rotation around <110> on the macroscopic scale (Fig. 6F–I). However, on the micron scale these can be shown to be twin boundaries (Fig. 6E).

5.2. Naturally deformed samples

Natural sample FJM01 exhibits a relatively homogenous brown colour (Fig. 7A), but CL reveals a quite complex growth stratigraphy (Fig. 7B). There is up to 0.5° of lattice misorientation per 100 μm (Fig. 7C) and it shows continuous crystallographic bending perpendicular to a single {111} plane and rotation around <011> (Fig. 7D, E). IR analysis shows that the diamond is of Type IaAB, i.e. it contains both A and B centres. It has a nitrogen concentration of approximately 370 ppm, with around 40% as B centres. The intensity (integrated area) of the platelet band is ~65 cm^{-2}.

Natural sample FJM02 also exhibits a homogenous brown colour, similar to that seen in FJM01 (Fig. 8A). The fact that it was recovered as a fragment means that no morphological information can be

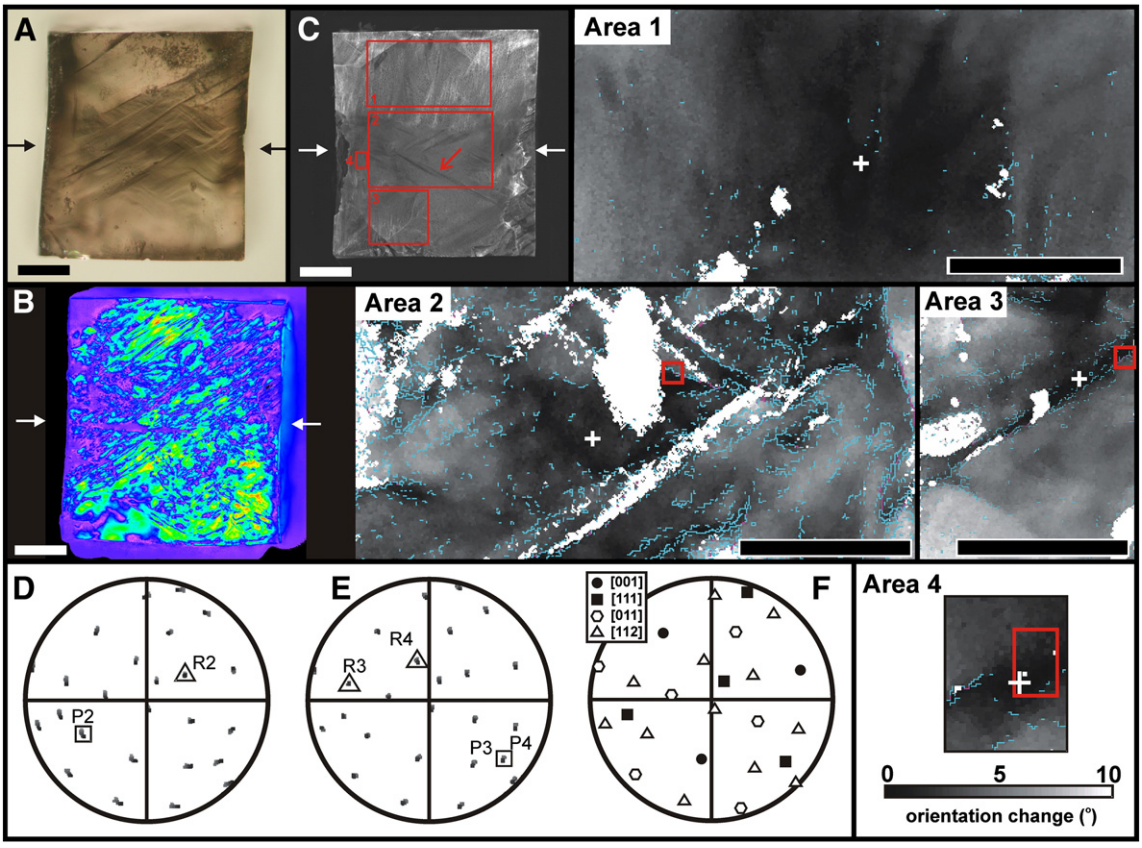

Fig. 3. Images and EBSD data of sample DD195 (Set II, uniaxial deformation) with viewing surface (111). (A) Photo taken under plane light. (B) MetriPol |sin (δ)| analysis of the same crystal face shown in (A). (C) CL image with four areas marked in red shown in subsequent EBSD maps. The arrows in (A–C) indicate the direction of uniaxial stress. The red arrow in (C) points to the curved lamellae deformation twins. Maps of Areas 1, 2, 3 and 4 are textural component maps; reference orientation is marked as white cross; aqua and purple lines signify 1 and 2° subgrain boundaries; scale bar is 200 μm in Areas 1–3 while Area 4 is 25 μm wide. The legend for crystal orientation range is given below Area 4 map. Red box in Areas 2–4 are the data regions represented in pole figures (D–F). (D) Pole figure showing poles to (111) slip planes (P2) and specific <112> rotation axes (R2) for both crystal bending and subgrain boundary directions in Area 2. (E) Pole figure of Area 3, the rotation axis (R3) and slip plane (P3) as determined by dispersion paths. This is also shown for Area 4 as well (P4, R4). (F) Reference pole figure showing the general location of main axes.

deduced. CL shows a quite simple growth stratigraphy with flat, consecutive layers of octahedral growth (Fig. 8B). There do appear to be some slightly bent lines cross-cutting the stratigraphy but these are not deformation twin lamellae. They probably are the result of polishing damage, or may reflect charging under the electron beam. There is up to 2° of lattice misorientation per 100 μm (Fig. 8C) and there is continuous crystallographic bending perpendicular to a single {111} plane (Fig. 8D, E). The axis of rotation is not completely resolved by the EBSD data, and is either around <011> or <112> (Fig. 8D, E). IR analysis shows that FJM02 is Type IaAB, with a nitrogen concentration of ~800 ppm, containing around 30% as B centres. The platelet intensity is ~100 cm^{-2}.

Platelets are interstitial carbon aggregates that are the by-product of the conversion of A to B centres [42]; there is a linear relationship between the amount of absorption created by B centres and the intensity (integrated area) of the platelet band [42]. Samples whose IR data lie on this linear trend are termed *regular*, while those whose data fall below this trend (i.e. decreased platelet intensity per B centre absorption) are termed *irregular*. Irregular platelet characteristics are thought to be the result of a heating and/or deformation event breaking up these interstitial aggregates [42], but as noted above, it remains unclear how the nitrogen defects are affected by these events. This further undermines the use of the nitrogen-aggregation data as an indicator of age/temperature of residence in the Earth for plastically deformed diamonds. Both of the natural diamonds in this study fall within the *irregular* category. Obviously, as the synthetic diamonds used in the experiments do not contain any nitrogen aggregation beyond A centres, this classification cannot be applied to them.

6. Discussion

As a result of deformation, single crystals of diamond behave similarly to other materials with FCC structure; they deform by activation of the {111}<011> slip system. In all of the deformation experiments presented in this study, these {111} planes dominate the deformation. However, since there are always at least two sets of these planes activated, significant cross-slip occurs. This results in a dominance of <112> rotation axes. Depending on which plane is dominant, different <112> rotation axes are utilized (cf. Figs. 3–6), confirming activation of the {111} <011> slip system. In diamond, the {111} plane is both the slip and the twin plane. The twins observed must have been deformation induced as no twins were observed before the HPHT experiments were performed.

This series of D-DIA experiments shows that twinning is an important mechanism for the accommodation of stress and strain in diamond. Here we clearly identified that the commonly observed {111} slip lamellae are in fact micro-twins that form under high pressure and temperature with minimal differential stress; they appear to represent the first step of the deformation process in these HPHT experiments. The generation of these twins in our quasi-hydrostatic (Set I)

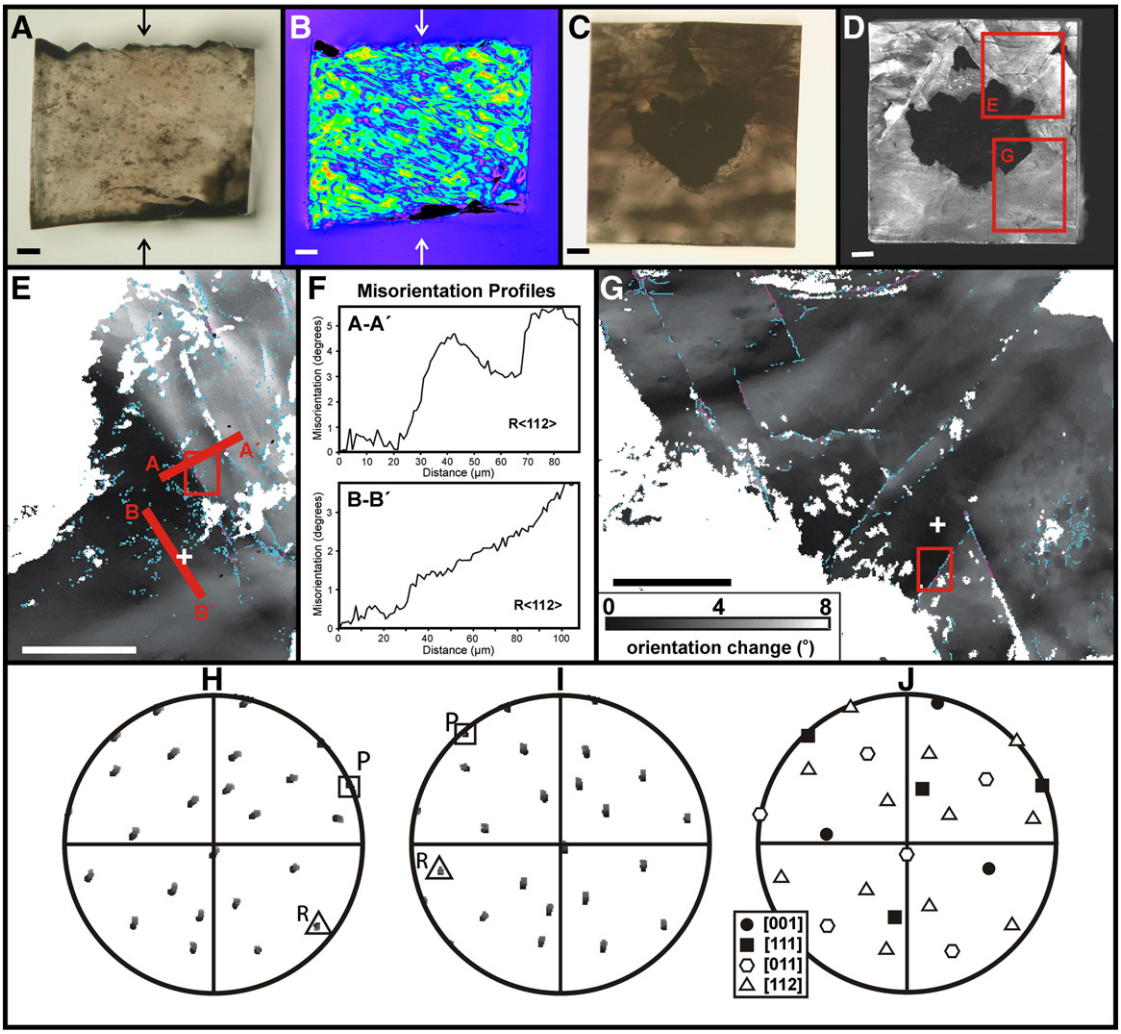

Fig. 4. Images and EBSD data of sample DD196 (Set II, uniaxial deformation). (A) Photo taken under plane light, viewing a $(0\bar{1}1)$ face. (B) MetriPol |sin (δ)| analysis of the same crystal face as shown in (A). Arrows in images (A) and (B) represent the uniaxial stress direction. (C) Plane light image of the crystal's bottom face (011) where the centre of sample has experienced severe surface damage due to the alumina piston applying the uniaxial stress. (D) CL image of the same crystal face shown in image (C); the red areas mark out the EBSD maps shown in images (E) and (G). Scale bars in (A–D) all represent 100 μm. (E). Textural component map for area 1; scale bar is 100 μm with 1 μm step size; reference orientation is marked as white cross; aqua and purple lines signify 1 and 2° subgrain boundaries. (F) Misorientation profiles of the two transects marked by red lines in (E). (G) Textural component maps for area 2; scale bar is 100 μm with 1 μm step size; reference orientation is marked as white cross; aqua and purple lines signify 1 and 2° subgrain boundaries; legend for colour coding of (F) and (G) shown. (H) Pole figure of data from red box in (E) representing crystal bending. Dispersion paths are consistent with (111) slip planes (P) and specific <112> rotation axes (R). (I) Pole figure of data from red box in (G) representing subgrain characteristics. Again, dispersion paths are consistent with (111) slip planes (P) and specific <112> rotation axes (R). (J) Reference pole figure showing the general location of main axes.

experiments probably reflects the mechanical anisotropy within the cell assembly. The fact that only minor lattice misorientation (<1° over 100 μm) was recorded in the Set I experiments is consistent with the samples maintaining their straight-edged appearances. The fact that the twin lamellae are themselves bent and kinked in the uniaxially deformed (Set II) experiments confirms that their formation was the first step in the deformation process, followed by ductile deformation. This bending, or kinking of the twin lamellae has been documented in naturally deformed diamonds [10].

The three samples deformed at the same strain rate (DD195, DD196 and DD197) all contained peak lattice misorientations in the centre of the sample and close to the faces at which the uniaxial stress was applied. However, the maximum change in orientation varies from 4° to 7° to 10° per 100 μm for samples DD197, DD196, and DD195, respectively (Table 2). It should be noted though that for DD196 the centre of the grain could not be observed; thus the maximum crystal bending was probably 2–3° higher than 7°. Interestingly, samples DD195 and DD197 have experienced very similar finite strain. However, the samples are orientated differently with respect to the principal stress direction (see Table 1), have different nitrogen concentrations, and were deformed at different confining pressures. These differences resulted in a more evenly distributed deformation in sample DD197, while in sample DD195 deformation was focussed in the centre of the crystal. The higher confining pressure may have assisted in focussing strain in the centre as slip along the sides of the sample was more restricted [43].

DD198 was deformed at higher strain rates and exhibits higher finite strain (6.1%) than the other samples. This resulted in maximum crystallographic bending of 18° per 100 μm. DD198 exhibits internal boundaries reaching up to 12° misorientation, compared to the other three samples (DD195, DD196 and DD197) where subgrain boundaries of 1° to 2° are observed. Furthermore, the twin lamellae are significantly bent due to increased plastic deformation. We suggest that the higher strain rate resulted in proportionally higher dislocation density, while the rapid recovery from the HPHT conditions resulted in the retention of the high-angle boundaries.

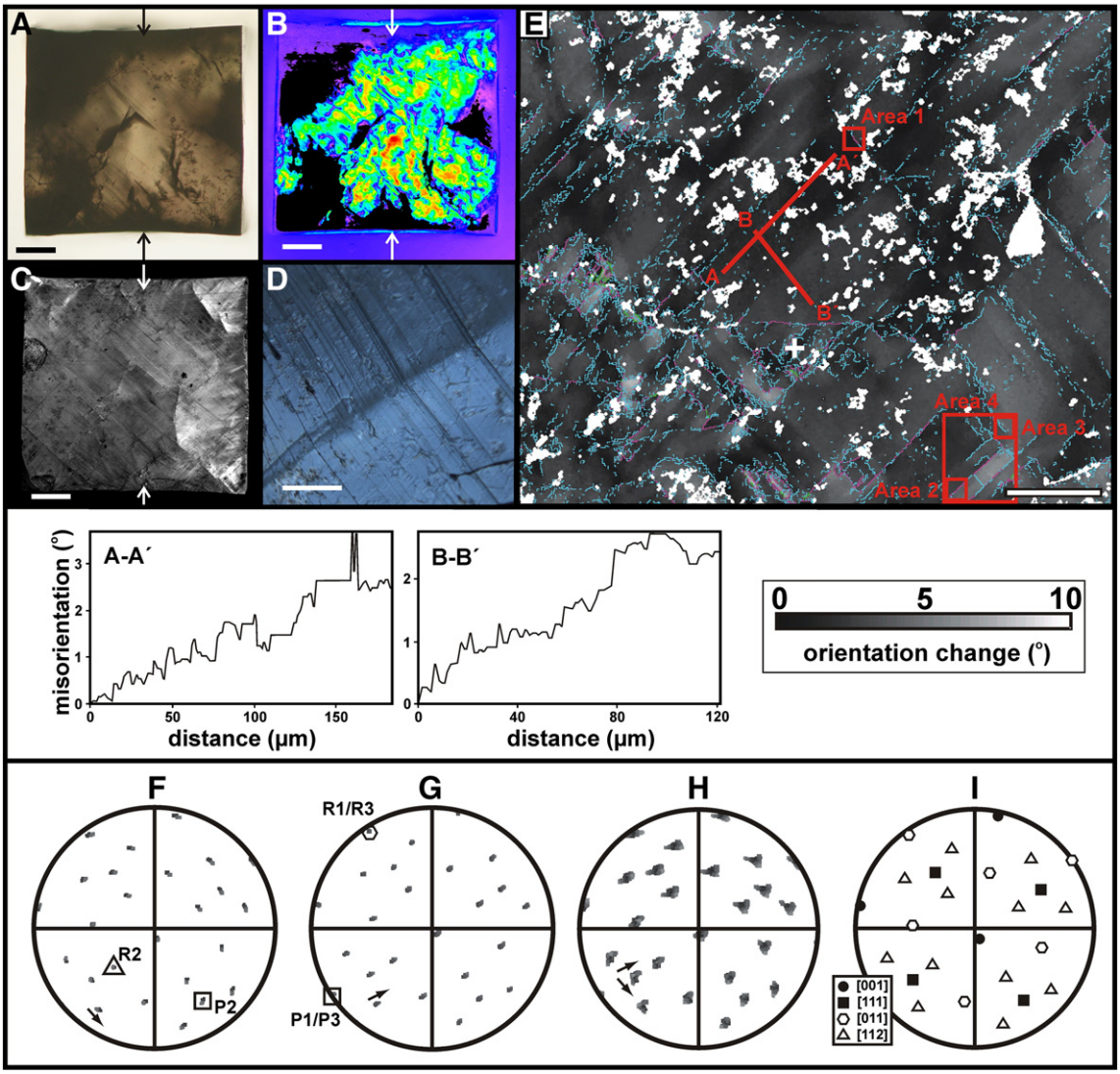

Fig. 5. Images and EBSD data of DD197 (Set II, uniaxial deformation) with viewing surface (001). (A) Photo taken under plane light. (B) MetriPol |sin (δ)| analysis of the same crystal face shown in (A). (C) CL image of the same crystal face shown in (A) and (B). The arrows in (A–C) indicate the direction of uniaxial stress; scale bars represent 200 μm. (D) Enlarged image showing the bending of the deformation twin lamellae; scale bar represents 100 μm. (E) Textural component maps for whole sample; scale bar is 100 μm; reference orientation is marked as white cross; aqua and purple line signify 1 and 2° subgrain boundaries. Two transects are marked with red lines and shown in the graphs below (A–E), along with the colour coding legend for (E). The red boxes mark out the data that is featured in the pole figures below (F–I) showing poles to (111) slip planes (P) and specific <112> and <011> rotation axes (R) for both crystal bending and subgrain boundary directions in area 2 (F), area 1 and 3 (G) and area 4 (H), which contains the trends seen in both areas 2 and 3 (marked by arrows). (I) Reference pole figure showing the general location of main axes.

While the mechanism of plastic deformation induced in these HPHT experiments is consistent with our knowledge of diamonds, the amount of lattice distortion generated is more than that seen in the naturally deformed samples studied here. This is to be expected; the strain rates applied to the experimental samples are much higher than those expected to occur in the mantle. Such high strain rates will favour generation of high dislocation densities and therefore high lattice distortions [44]. This is due to the fact that at high strain rates, annihilation of dislocations is insignificant compared to the generation of new ones. Nevertheless, the principal slip system observed in the experimental samples is the same as that activated in the two natural diamonds. Interestingly, in the natural sample FJM02, it is possible that only one of the {111} slip planes is activated and the rotation axis is [011] (Fig. 8D, E). This confirms that if several slip planes are activated, as in the Set II experiments and FJM01, cross-slip and climb occur and rotation occurs more dominantly around [112].

As discussed above, the occurrence of plastic deformation in diamonds has long been associated with both brown and pink colour in diamonds. While the exact cause (i.e. the specific defect responsible for the relevant absorption) of the pink colour is unknown, a model involving vacancy clusters has been proposed as the cause of brown colour [45]. While the data presented in this study do not shed any light on the exact cause of either colour, it is clear that slip and the generation of {111} twin lamellae are possible without the creation of any colour, as seen in the Set I experiments. The Set II experiments all showed varying levels of brown colour, but due to the abundance of multiple slip planes, no colour graining was observed. Also, the natural diamonds contained relatively homogenous brown colour without any deformation twin lamellae being present.

In general, deformation twin lamellae in diamonds are very poorly described in the literature. Many early studies [10,46] placed more interest in the etch pits that decorate these {111} lamellae. Varma [10] stated that, compared to experimentally deformed samples of diamond or diamond-like structures, the {111} lamellae were far less abundant in natural samples, commonly separated by several microns. Shiryaev et al. [12] used high-resolution transmission electron microscopy

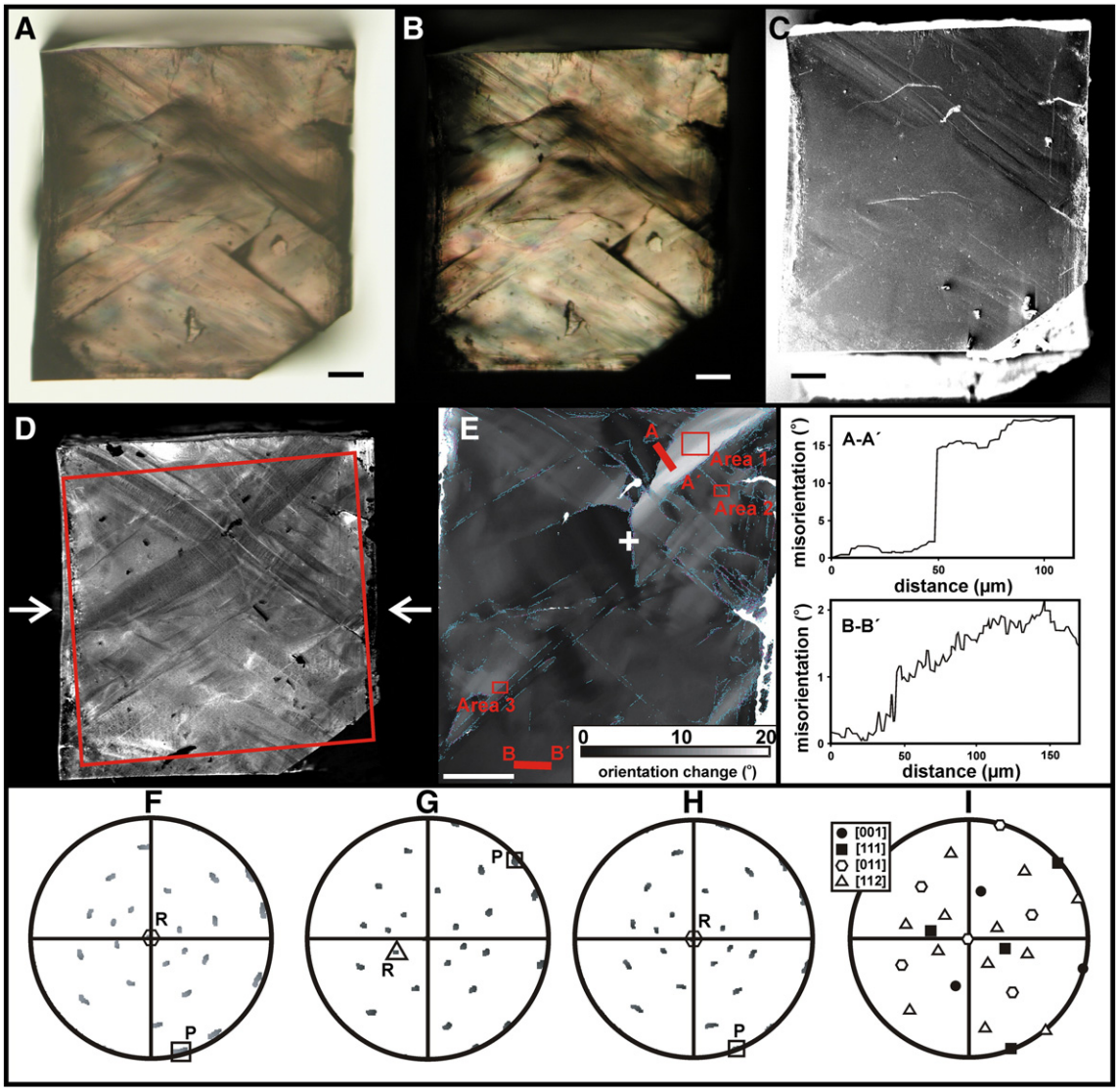

Fig. 6. Images and EBSD data of DD198 (Set II, uniaxial deformation), all viewing the same $(0\bar{1}1)$ crystal face. (A) Photo taken under plane light. (B) Photo taken between crossed polarizers. (C) An SE image. (D) A CL image with white arrows marking the uniaxial stress direction. Note bending of the deformation twin lamellae. Red box marks out EBSD map shown in (E). (E) Textural component maps for whole sample; reference orientation is marked as white cross; aqua and purple lines signify 1 and 2° subgrain boundaries; scale bar 200 μm with step sizes of 1 μm, colour coding legend shown in bottom right corner. Two transects are marked with red lines and shown next to (E). The red boxes labelled Areas 1–3 are presented in the pole figures (F–H). (F) Pole figure showing poles to (111) slip planes (P) and specific <112> and <011> rotation axes (R) for both crystal bending and subgrain boundary directions for Area 1; (G) is for Area 2 and (H) is for Area 3. (I) Reference pole figure showing the general location of main axes.

(HR-TEM) to identify a single mechanical twin plane, but did not resolve any more or describe their abundances. A recent study of twin lamellae in natural pink diamonds by Gaillou et al. [13] provides the best description of these features. In their study of nineteen rough, gem-quality pink diamonds, Gaillou et al. [13] observed that the lamellae were between 0.8 and 1 μm wide, but contained multiple twin domains. In all the lamellae, the twins occur as pairs. This is something also seen in all of our experimental samples and is characteristic of "gliding twins" [47]. TEM analysis of one 770 nm-wide lamella by Gaillou et al. [13] showed that it contained six twin domains. It is within these lamellae that the pink colour (graining) is observed. This concentration of colour in the {111} lamellae is also reported for brown colour in many natural diamonds [45,48]. The more coloured lamellae present, the more intense the colour of the diamond [13]. The deformation twin lamellae observed in the experimental samples from this study have a similar width as previously reported and also occur in pairs. However there is a lack of multiple twin domains within the individual lamellae in our samples. It is unknown whether this is the reason for the absence of obvious graining, but it is thought to be more likely to be due to the activation of multiple {111} slip planes masking the effect.

It is interesting that neither of the two natural samples analysed in this study showed any evidence of containing deformation twin lamellae. While the results of the experiments show that the formation of twin lamellae is the first step in the deformation process, followed by crystal lattice distortion, this is not necessarily the case in natural diamonds. It is possible that very small strain rates over hundreds of million years allow for small amounts of lattice distortion without the generation of deformation twins. Unfortunately there are no EBSD data from natural plastically-deformed diamonds in the literature for comparison. To the authors' knowledge, only Cayzer et al. [15] have published quantitative deformation data on diamonds; they used EBSD to analyze the diamond surrounding inclusions suspected of having a lower mantle origin. They showed that the over-pressure created by the expansion and resultant phase change

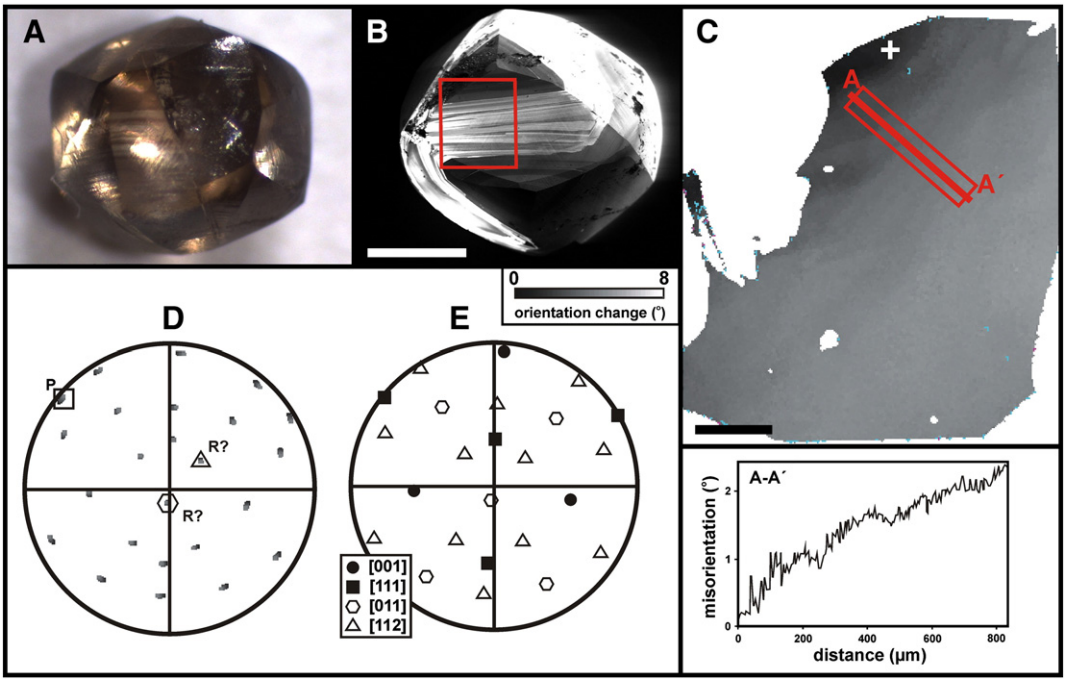

Fig. 7. Images and EBSD data of natural sample FJM01. (A) Image taken under plane light. (B) CL image of the same crystal face shown in A. Scale bar is 0.5 mm. (C) Textural component map with maximum orientation spread of 8° (see legend), white cross marks reference orientation, step size is 2 μm. Scale bar represents 100 μm. Red line A–A′ defines transect shown in graph showing orientation change across grain. (D) Pole figure of EBSD data collected from the red box shown in (C), in which rotation axis (R) and pole of slip plane (P) are marked. Note that two possible rotation axes, [011] and [112], are marked on the figure as the data is not totally conclusive. (E) Reference pole figure for main axes shown in (D).

of the minerals resulted in a maximum crystal orientation change of 7° in the immediate vicinity of the inclusions, an amount well within that achieved by the D-DIA experiments.

This study highlights the power of EBSD for the investigation of plastic deformation in diamonds. A broad analytical programme is required to confirm the amounts of lattice distortion seen in naturally deformed diamonds; this may show some quantifiable differences between pink and brown diamonds, as well as naturally annealed colourless but deformed diamonds. It will also help to provide further characteristics of the deformation twin lamellae in natural diamonds

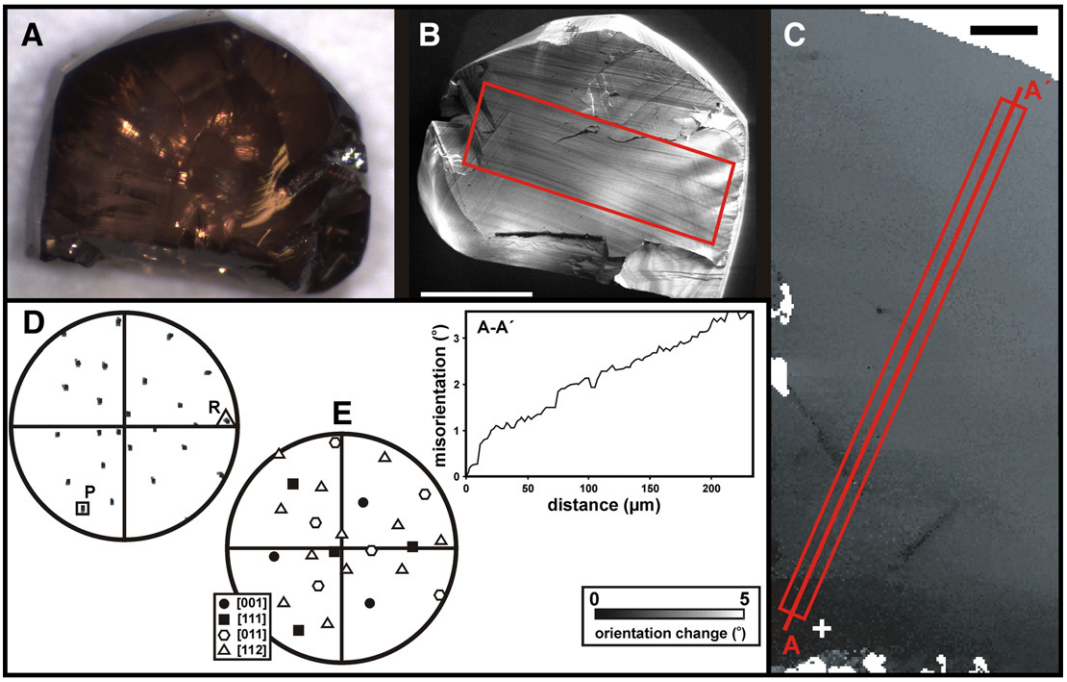

Fig. 8. Images and EBSD data of natural sample FJM02. (A) Image taken under plane light. (B) CL image of the same crystal face shown in (A). Scale bar is 0.5 mm. (C) Textural component map with maximum orientation spread of 5°, white cross marks reference orientation, step size is 3 μm. Scale bar represents 100 μm. Red line A–A′ defines transect shown in graph below (C), showing a continuous change in orientation of 3° over a distance of 240 μm. (D) Pole figure of EBSD data collected from the red box in (C), in which rotation axis (R) and pole of slip plane (P) are marked. (E) Reference pole figure for main axes seen in (D).

(size, frequency, distribution) and whether their absence in brown and pink diamonds is common. Combining this technique and the subsequent dataset with a more extensive HPHT experimental programme may provide insights into the P, T and stress regimes responsible for specific deformation features observed in natural diamonds. This could give us a clearer understanding of the events that deform diamonds within the Earth, and when in the diamond's history these events occur.

7. Conclusions

We report the first study of its kind to apply the D-DIA HPHT experimental apparatus in the investigation of plastic deformation of diamond under mantle-like conditions. It is clear from the data presented that the experimental technique used has been successful in its primary objective of deforming diamond. Also, the structures formed during the experiments, namely the {111} twin lamellae, have exactly the same characteristics as those reported in naturally deformed diamonds [8–10,12,13]. Detailed EBSD analysis shows that the commonly reported {111} slip lines are in fact deformation twins with a width of 300 to 700 nm and a spacing of ~1 to 20 μm. These twins form as a first response to differential stress under the experimental HPHT conditions with very little subsequent lattice bending (<1° per 100 μm). Further differential stress results in continuous crystal bending (4–18° per 100 μm) including bending of the {111} twin lamellae and formation of low-angle and high-angle boundaries. At the same P and T conditions, higher strain rates result in higher misorientations across newly formed boundaries. In all experiments, dislocations and associated crystal lattice bending, as well as low- and high-angle boundaries, are dominantly related to the slip system {111}<110>. When slip occurs on multiple {111} planes, rotation occurs around <112> axes.

EBSD analysis of two natural brown diamonds (0.5–2° lattice bending per 100 μm) suggests that the amount of lattice misorientation created in the experiments is probably in excess of what is achieved in nature. Also, no deformation twin lamellae were observed in the two natural samples. While this study has shown the power of EBSD analysis for an investigation of plastic deformation in diamond, there are few data with which to compare our results. So it is unknown whether deformation twin lamellae are present in almost all naturally deformed diamonds, or whether it is common for deformation to occur without their initial generation. Far more EBSD analysis is required to confirm the amounts of lattice distortion seen in naturally deformed diamonds, as well as the characteristics of the deformation twin lamellae in natural diamonds (size, frequency, distribution). Furthermore, the study reported here shows that a combined analytical (CL, SE and birefringence imaging, IR spectroscopy as well as EBSD) and experimental approach offers the opportunity to markedly improve our understanding of the effects of plastic deformation on nitrogen aggregation, impurity and defect migration in diamonds and provide a database for possible strain rate estimates for naturally deformed diamonds.

Acknowledgements

DH wishes to thank EPSRC and DTC for funding of his PhD during which, the bulk of this research was carried out, as well as the short term Marie Curie Studentship during which the experiments were performed at BGI. DTC and the Large Single Crystal Synthesis group at Element Six are also thanked for providing the synthetic samples. Hubert Schulze (BGI) is thanked for his technical expertise in preparing materials for the cell assembly and post experimental recovery of the samples. The following people are thanked for their constructive input during earlier versions of this manuscript; Sue O'Reilly, Jeff Harris, John Chapman and Andrei Shiryaev. Judith Milledge is thanked for providing the natural samples. The authors acknowledge the facilities, and the scientific and technical assistance, of the Australian Microscopy and Microanalysis Research Facility at the ACMM, Sydney University. Some of the analytical data were obtained using instrumentation funded by the DEST Systemic Infrastructure Grants, ARC LIEF, NCRIS, industry partners and Macquarie University. This is contribution 211 from the ARC Centre of Excellence for Core to Crust Fluid Systems (www.ccfs.mq.edu.au) and 850 from the GEMOC Key Centre (www.gemoc.mq.edu.au).

References

[1] T. Stachel, J.W. Harris, Ore Geol. Rev. 34 (2008) 5–32.
[2] A.T. Collins, J. Gemmol. 18 (1982) 37–75.
[3] A.T. Collins, H. Kanda, H. Kitawaki, Diamond Relat. Mater. 9 (2000) 113–122.
[4] A. Yacoot, M. Moore, W.G. Machado, J. Appl. Crystallogr. 31 (1998) 767–776.
[5] W.G. Machado, M. Moore, A. Yacoot, J. Appl. Crystallogr. 31 (1998) 777–782.
[6] E.L. Tomlinson, D. Howell, A.P. Jones, D.J. Frost, Diamond Relat. Mater. 20 (2011) 11–17.
[7] J.W. Christian, S. Mahajan, Prog. Mater. Sci. 39 (1995) 1–157.
[8] C. Phaal, Philos. Mag. 10 (1964) 887–891.
[9] R.C. De Vries, Mater. Res. Bull. 10 (1975) 1193–1200.
[10] C.K.R. Varma, Acta Metall. 18 (1970) 1113–1119.
[11] Yu.L. Orlov, The mineralogy of the Diamond, John Wiley, New York, 1977.
[12] A.A. Shiryaev, D.J. Frost, F. Langenhorst, Diamond Relat. Mater. 16 (2007) 503–511.
[13] E. Gaillou, J.E. Post, N.D. Bassim, A.M. Zaitsev, T. Rose, M.D. Fries, R.M. Stroud, A. Steele, J.E. Butler, Diamond Relat. Mater. 19 (2010) 1207–1220.
[14] D.J. Prior, A.P. Boyle, F. Brenker, M.C. Cheadle, A. Day, G. Lopez, L. Peruzzo, G.J. Potts, S. Reddy, R. Spiess, N.E. Timms, P. Trimby, J. Wheeler, L. Zetterström, Am. Mineral. 84 (1999) 1741–1759.
[15] N.J. Cayzer, S. Odake, B. Harte, H. Kagi, Eur. J. Mineral. 20 (2008) 333–339.
[16] F.V. Kaminsky, G.K. Khachatryan, Lithos 77 (2004) 255–271.
[17] L.A. Taylor, M. Anand, Chem. Erde 64 (2004) 1–74.
[18] D. Howell, Eur. J. Mineral. 24 (2012) 575–585.
[19] L. Nasdala, F.E. Brenker, J. Glinnemann, W. Hofmeister, T. Gasparik, J.W. Harris, T. Stachel, I. Reese, Eur. J. Mineral. 15 (2003) 931–935.
[20] L. Nasdala, W. Hofmeister, J.W. Harris, J. Glinnemann, Am. Mineral. 90 (2005) 745–748.
[21] Y.V. Babich, B.N. Feigelson, Inorg. Mater. 45 (2009) 616–619.
[22] Y.V. Babich, B.N. Feigelson, Geochem. Int. 47 (2009) 94–98.
[23] D. Howell, C.J. O'Neill, K.J. Grant, W.L. Griffin, N.J. Pearson, S.Y. O'Reilly, Diamond Relat. Mater. 29 (2012) 29–36.
[24] D. Howell, C. O'Neill, K. Grant, W.L. Griffin, S.Y. O'Reilly, N. J. Pearson, R. Stern, T. Stachel, Platelet development in cuboid diamonds: insights from μ-FTIR mapping, Contrib. Mineral. Pet. (in press) http://dx.doi.org/10.1007/s00410-012-0786-9.
[25] H.J. Frost, M.F. Ashby, in: Pergamon Press, 1982, p. 165.
[26] T. Evans, J.W. Harris, in: J. Ross (Ed.), Kimberlites and related rocks, vol. 2, Blackwell Scientific Publications, Melbourne, 1989, pp. 1001–1006.
[27] M.J. Mendelssohn, H.J. Milledge, Int. Geol. Rev. 37 (1995) 95–110.
[28] K.S. Byrne, J.D. Anstie, J. Chapman, A.N. Luiten, Diamond Relat. Mater. 23 (2012) 125–129.
[29] H.-W. Chen, V. Rudolph, Diamond Relat. Mater. 12 (2003) 1633–1639.
[30] T. Liu, D. Raabe, S. Zaefferer, Sci. Technol. Adv. Mater. 9 (2008) 035013.
[31] E.V. Rubanova, W.L. Griffin, S. Piazolo, S.Y. O'Reilly, T. Stachel, R. Stern, A.C. Birnie, in: 10th International Kimberlite Conference Proceedings, 176, 2012.
[32] E.V. Rubanova, S. Piazolo, W.L. Griffin, S.Y. O'Reilly, Deformation microstructures reveal a complex mantle history for polycrystalline diamond, Geochem. Geophys. Geosyst. (in press) http://dx.doi.org/10.1029/2012GC004250.
[33] Y. Wang, W.B. Durham, I.C. Getting, D.J. Weidner, Rev. Sci. Instrum. 74 (2003) 3002–3011.
[34] A.M. Glazer, J.G. Lewis, W. Kaminsky, Proc. R. Soc. Lond. 452 (1996) 2751–2765.
[35] G. Schubert, D.L. Turcotte, P. Olson, Mantle convection in the Earth and Planets, Cambridge University Press, Cambridge, 2001.
[36] D.J. Prior, J. Wheeler, L. Peruzzo, R. Spiess, C. Storey, J. Struct. Geol. 24 (2002) 999–1011.
[37] M. Bestmann, D.J. Prior, J. Struct. Geol. 25 (2003) 1597–1613.
[38] J. Wheeler, D.J. Prior, Z. Jiang, R. Spiess, P. Trimby, Contrib. Mineral. Petrol. 141 (2001) 109–124.
[39] C.D. Barrie, A.P. Boyle, S.F. Cox, D.J. Prior, Mineral. Mag. 72 (2008) 1181–1199.
[40] S. Reddy, N. Timms, W. Pantleon, P. Trimby, Contrib. Mineral. Petrol. 153 (2007) 625–645.
[41] S. Piazolo, M. Montagnat, J.R. Blackford, J. Microscopy 230 (2008) 509–519.
[42] G.S. Woods, Proc. R. Soc. Lond. 407 (1986) 219–238.
[43] E. Mariani, J. Mecklenburgh, J. Wheeler, D.J. Prior, F. Heidelbach, Acta Mater. 57 (2009) 1886–1898.
[44] M.F. Ashby, Philos. Mag. 21 (1970) 399–424.
[45] D. Fisher, Lithos 112 (2009) 619–624.
[46] S. Tolansky, A. Halperin, S.H. Emara, Philos. Mag. 3 (1958) 675–679.
[47] M.J. Buerger, J. Miner. Soc. Am. 30 (1945) 469–482.
[48] D. Fisher, S.J. Sibley, C.J. Kelly, J. Phys. Condens. Matter 21 (2009) 364213.